ANNUAL REVIEWS

Annual Review of Condensed Matter Physics

Monte Carlo Studies of Quantum Critical Metals

Erez Berg,[1] Samuel Lederer,[2] Yoni Schattner,[3,4] and Simon Trebst[5]

[1]Department of Physics, James Franck Institute, University of Chicago, Chicago, Illinois 60637, USA; email: berge@uchicago.edu

[2]Department of Physics, Massachusetts Institute of Technology, Cambridge, Massachusetts 02139, USA

[3]Department of Physics, Stanford University, Stanford, California 94305, USA

[4]Stanford Institute for Materials and Energy Sciences, SLAC National Accelerator Laboratory and Stanford University, Menlo Park, California 94025, USA

[5]Institute for Theoretical Physics, University of Cologne, Cologne 50937, Germany

Annu. Rev. Condens. Matter Phys. 2019. 10:63–84

First published as a Review in Advance on November 16, 2018

The *Annual Review of Condensed Matter Physics* is online at conmatphys.annualreviews.org

https://doi.org/10.1146/annurev-conmatphys-031218-013339

Keywords

superconductivity, non-Fermi liquid, Ising nematic order, spin-density wave order, quantum Monte Carlo

Abstract

Metallic quantum critical phenomena are believed to play a key role in many strongly correlated materials, including high-temperature superconductors. Theoretically, the problem of quantum criticality in the presence of a Fermi surface has proven to be highly challenging. However, it has recently been realized that many models used to describe such systems are amenable to numerically exact solution by quantum Monte Carlo (QMC) techniques, without suffering from the fermion sign problem. In this review, we examine the status of the understanding of metallic quantum criticality and the recent progress made by QMC simulations. We focus on the cases of spin-density wave and Ising nematic criticality. We describe the results obtained so far and their implications for superconductivity, non-Fermi liquid behavior, and transport near metallic quantum critical points. Some of the outstanding puzzles and future directions are highlighted.

1. INTRODUCTION

One of the ubiquitous properties of strongly correlated materials is the presence of different electronically ordered states in close competition with each other, which can be tuned by relatively small changes in a tuning parameter such as pressure, material composition, or magnetic field. Another common feature of these systems is an anomalous metallic state whose properties are incompatible with Fermi liquid theory. An appealing scenario to account for the latter observation is that it originates from an underlying quantum critical point (QCP) at which the metallic ground state becomes unstable toward some form of order. In this scenario, the behavior of the anomalous metallic state thus reflects its proximity to a non-Fermi liquid fixed point, which governs the system's properties over a broad range of temperatures and tuning parameters.

There is ample experimental evidence that some sort of quantum criticality is present in many materials, such as heavy fermion compounds (1–10), iron-based superconductors (11–17), and electron-doped cuprate superconductors (18, 19). In the hole-doped cuprates the situation is less clear, although there is some evidence for a QCP underneath the superconducting (SC) dome in these systems (20–22). In all these systems, a fan-shaped metallic regime emanates from the (putative) QCP, often featuring, among other phenomena, anomalous power laws in the temperature (T) dependence of the electrical resistivity. (Rather than the T^2 behavior of Fermi liquid theory, the resistivity in the putative quantum critical regime is often linear in T.[1]) In almost all the above systems, an unconventional SC phase emerges with a maximum transition temperature close to the apparent QCP, indicating an intimate connection between quantum criticality and superconductivity.

The theory of quantum criticality in metals is a decades-old problem, dating back to the seminal works of Hertz (24), Moriya (25), and Millis (26). The problem has proven challenging due to the profusion of low-energy degrees of freedom. Unlike classical critical phenomena and QCPs in insulators, in which the correlations typically become singular only at a single point in momentum space, in the metallic case the low-energy degrees of freedom live on an entire extended manifold of momenta—the Fermi surface.[2] As we elaborate below, despite intense work on the topic and significant technical progress (30–63), there is no accepted theory to describe quantum criticality in systems with a Fermi surface.

In recent years, it has been appreciated that many paradigmatic models of metallic criticality can be solved (64–74) by quantum Monte Carlo (QMC) simulations without suffering from the notorious sign problem (75), which often hinders QMC simulations in systems of interacting fermions. This opens the way for fully controlled and numerically exact solutions of models of quantum critical metals, providing a nonperturbative handle on the problem. Beyond their quantitative guidance, these numerical solutions are useful both as a benchmark for existing theoretical descriptions and as a guide for new ones. The purpose of this review is to examine the status of the theory of metallic quantum criticality, focusing on the recent progress made and questions raised by sign-problem-free QMC simulations and their implications for our current understanding of this problem.

2. SETUP OF THE PROBLEM

We start with a discussion of general theoretical considerations for the problem of metallic quantum criticality. We present a (presumably) generic field theoretical description of such QCPs and

[1] Other power laws are seen in certain systems. See, for example, References 7, 8, and 23.

[2] The situation is different in semimetals, for instance, systems with a Dirac dispersion, where the Fermi surface consists of only one point. In these systems, much theoretical progress has been made; see, e.g., References 27–29.

review briefly the various analytical techniques applied to it before turning to the numerical QMC approach in the next section.

2.1. General Considerations and Field-Theoretical Model

Consider a lattice model of fermions, coupled via a general short-range interaction. For a generic dispersion of the fermions (i.e., without the Fermi surface fine-tuned to perfect nesting or a van Hove singularity), the model is stable when interactions are infinitesimally weak except for a possible SC instability. Thus, any QCP at which an ordered state forms out of the metal must occur at finite strength of the coupling. From this perspective, the problem of metallic quantum criticality is intrinsically an intermediate coupling problem and may be not accessible via methods that are perturbative in the interaction strength.

To enable a perturbative approach to the critical point, we may introduce a fluctuating order parameter field by hand, tune it to the vicinity of a symmetry-breaking transition, and consider the effects of a small coupling between the order parameter fluctuations and the fermions. Schematically, the system is described by the following Euclidean action:

$$S = S_\psi + S_\phi + S_{\rm int}, \qquad 1.$$

where

$$\begin{aligned} S_\psi &= \int_0^\beta d\tau \sum_{\mathbf{k}} \psi^\dagger_{\mathbf{k}} (\partial_\tau + \varepsilon_{\mathbf{k}} - \mu)\, \psi_{\mathbf{k}}, \\ S_\phi &= \int_0^\beta d\tau \int d^d x \left[\frac{1}{2} r\phi^2 + \frac{1}{2}(\nabla\phi)^2 + \frac{1}{2c^2}(\partial_\tau \phi)^2 + \frac{u}{4}\phi^4 + \ldots \right]. \end{aligned} \qquad 2.$$

Here, the fermionic action S_ψ is given in terms of the fermionic operators, $\psi^\dagger$ and ψ (which in general may have spin and other indices, not displayed here), with dispersion $\varepsilon_{\mathbf{k}}$ and chemical potential μ. The bosonic action, S_ϕ, is the usual Landau–Ginzburg–Wilson action, written as an expansion in powers of the order parameter ϕ and its derivatives. The precise nature of ϕ depends on the symmetry broken in the ordered state (see explicit examples below). The tuning parameter r drives the system through a QCP. The interaction term, $S_{\rm int}$, is of the Yukawa form, linear in the order parameter and quadratic in the fermion operators, and includes a form factor that encodes the symmetry of the order parameter (see Equations 3 and 4 below). We focus on the case of $d = 2$ spatial dimensions, which is relevant to many materials of interest.

Throughout this review, we focus on two types of paradigmatic QCPs: a spin-density wave (SDW) QCP and an Ising-nematic QCP. An SDW QCP involves ordering at a nonzero wavevector $\mathbf{Q}$. For simplicity, we focus on the case of a commensurate ordering wavevector (antiferromagnetic order). The coupling of the order parameter to the fermions has the form

$$S_{\rm int} = \lambda \int d^2 x \int_0^\beta d\tau\, e^{i\mathbf{Q}\cdot\mathbf{x}} \vec{\phi}(\mathbf{x}) \cdot \psi^\dagger(\mathbf{x}) \vec{\sigma}\, \psi(\mathbf{x}) + h.c., \ \text{(SDW)}, \qquad 3.$$

where $\vec{\sigma}$ are spin Pauli matrices, and $\vec{\phi}$ is the SDW order parameter, which may be a one-, two-, or three-component vector (depending on whether the SDW order parameter has easy-axis, easy-plane, or isotropic character, respectively). The SDW order parameter couples particularly strongly to fermions in the vicinity of a discrete set of hot spots on the Fermi surface (or hot lines in $d = 3$ dimensions) that are connected to each other by the magnetic ordering wavevector $\mathbf{Q}$. At these points, fermions can scatter off the low-energy order parameter fluctuations while remaining on the Fermi surface. In the SDW ordered phase, a gap opens at and near the hot spots, causing reconstruction of the Fermi surface, as shown in **Figure 1*a*,*b***.

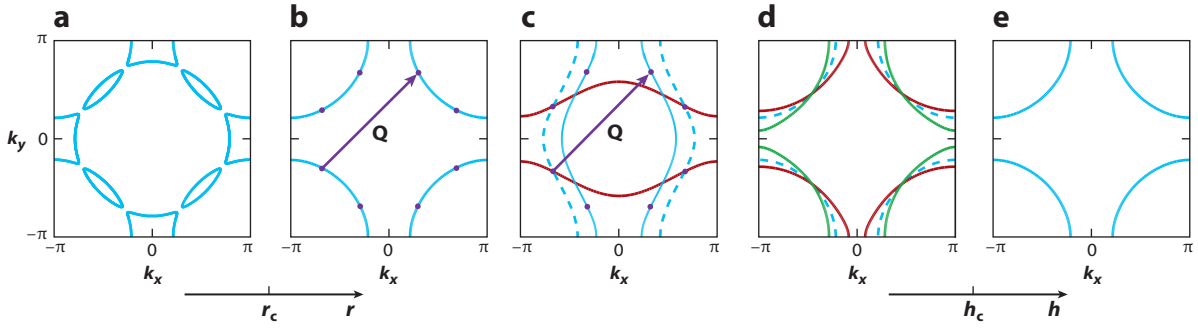

Figure 1

Evolution of the Fermi surface across the SDW transition (*a*,*b*) and the Ising-nematic transition (*d*,*e*). Panel *c* shows the band structure of the two-band model used in the quantum Monte Carlo simulations of an SDW transition (studied in References 67 and 68). The dashed line is the blue Fermi surface shifted by $\mathbf{Q} = (\pi, \pi)$. In panels *b* and *c*, the locations of the hot spots, connected by the magnetic ordering vector $\mathbf{Q} = (\pi, \pi)$, are indicated by the purple circles. In panels *d* and *e*, the blue line represents the Fermi surface in the disordered phase, and the green and red lines show the two possible configurations of the Fermi surface in the nematic phase. Abbreviation: SDW, spin-density wave.

A second type of QCP we consider is an Ising-nematic QCP, in which the point-group symmetry of the system is reduced from tetragonal to orthorhombic. This is a paradigmatic example of a $\mathbf{Q} = 0$ order parameter that preserves translational symmetry. The order parameter has two inequivalent configurations and is represented by an Ising-like scalar field that changes sign under rotation by 90°. The interaction term in the action reads as

$$S_{\text{int}} = \lambda \int d^2x \int_0^\beta d\tau \, \phi(\mathbf{x})\psi^\dagger(\mathbf{x})(\partial_x^2 - \partial_y^2)\psi(\mathbf{x}) \text{ (Ising nematic).} \quad 4.$$

In the ordered phase, $\phi \neq 0$, and the Fermi surface becomes elongated either along x or y (see **Figure 1*d*,*e***). Near the QCP, the small $\mathbf{Q}$ fluctuations of the order parameter couple strongly to fermions along the entire Fermi surface (with the exception of a discrete set of cold spots along the diagonals, where the coupling vanishes to leading order in ϕ).

2.2. Perturbative Expansions

In all cases, the coupling to the fermions λ is a relevant parameter in the sense that perturbation theory in λ breaks down at sufficiently low energy scales. It is nevertheless useful to start from the small λ limit, which can provide information about the crossover regime and give clues about the nature of the ground state.

Let us focus on the case of an Ising-nematic QCP, which is somewhat simpler to analyze. To leading order in λ, the bosonic field acquires a self-energy given by[3]

$$\Pi(\mathbf{q}, i\Omega_n) = -\lambda^2 \cos^2(2\theta_\mathbf{q}) \nu_0 \left[1 - \frac{|\Omega_n|}{\sqrt{\Omega_n^2 + (v_F^2 q^2)}} \right]. \quad 5.$$

Here, ν_0 and v_F are, respectively, the density of states of the fermions at the Fermi level and their Fermi velocity, and $\theta_\mathbf{q}$ is the angle between $\mathbf{q}$ and the x axis. For simplicity, we have assumed a circular, isotropic Fermi surface. The angular dependence of Equation 5 comes from the anisotropy

[3] Here, we set the units such that λ^2 has dimensions of energy.

of the Yukawa coupling (Equation 4). Note that Equation 5 vanishes along the diagonals $q_x = \pm q_y$; this is a consequence of the cold spots, where the coupling constant between ϕ and the fermions vanishes.

At sufficiently low frequency, the $|\Omega_n|$ term in Equation 5 becomes dominant over the Ω_n^2/c^2 term in Equation 2. The crossover scale where this occurs can be roughly estimated by equating the frequency-dependent part of Equation 5 to the bare inverse ϕ propagator, assuming that $|\mathbf{q}| \sim \Omega_n/c$. The resulting crossover scale is

$$\Omega_b = |\lambda|\sqrt{v_0 c^3/v_F}. \quad 6.$$

At frequencies below Ω_b, the boson dynamics is dominated by the Landau damping term, which is proportional to $|\Omega_n|/(v_F q)$, and the dynamical critical exponent z increases from 1 to 3.

Next, we consider the lowest-order contribution of the boson on the fermion self-energy. We focus on frequencies $\omega_n \ll \Omega_b$, where we should use the dressed form of the boson propagator, including its self-energy (Equation 5).[4] To order λ^2, the self-energy on the Fermi surface is given by

$$\Sigma(\mathbf{k}_F, \omega_n) \sim -i(\lambda^4 \sin^4 \theta_{\mathbf{k}_F}/E_F)^{1/3}|\omega_n|^{2/3}\mathrm{sgn}(\omega_n), \quad 7.$$

where $E_F \sim v_0 v_F^2$ is the Fermi energy, and $\theta_{\mathbf{k}_F}$ is the angle between the fermion's momentum and the x axis. The fermions thus become strongly damped by the coupling to the bosonic fluctuations almost everywhere on the Fermi surface (except for the cold spots where $\theta_{\mathbf{k}_F} = \pm\pi/4$), with a damping rate that scales as $\omega^{2/3}$ [compared with $\omega^2 \log(1/\omega)$ in an ordinary two-dimensional Fermi liquid].

From Equation 7, we can estimate the scale at which Fermi liquid behavior breaks down. As for the bosons, this is done by equating the self-energy (Equation 7) to the $i\omega_n$ term in the bare fermion inverse propagator. This procedure gives

$$\Omega_{NFL} = \frac{\lambda^4}{E_F}. \quad 8.$$

Note that for small λ, $\Omega_{NFL} \ll \Omega_b$. Thus, there is a parametrically broad window of energies between Ω_{NFL} and Ω_b in which the bosons are described by overdamped dynamics (with a dynamical critical exponent $z = 3$), but the feedback of the bosons on the fermions is weak. This justifies the use of the zeroth-order fermionic polarization bubble in the evaluation of Equation 5.

At frequencies below Ω_{NFL}, one can no longer ignore the fermion self-energy. Higher-order corrections to Σ are increasingly singular at low frequencies. Extending the problem to the case of a large number N of fermion flavors does not solve this problem, because a large set of diagrams that are naively subleading in powers of $1/N$ are in fact divergent and must be treated on equal footing (45, 47). There is currently no understanding of the resulting fixed point. The $1/N$ expansion similarly fails in the SDW QCP problem (48).

Other modifications of the problem have been devised to gain control of calculations (49, 51, 58, 76). These methods, which we do not review here, involve various large N limits, the introduction of nonlocal terms in the action, and the extension of the problem to fractional dimensions. The properties of the $d = 2$, finite-N problem remain unclear.

For the SDW problem, a strongly coupled fixed point has been found recently (60, 77). This fixed point has many unexpected properties, such as a dynamical critical exponent $z = 1$; emergent nesting at the hot spots; and a singular, anisotropic boson dispersion in the infrared.

[4]The existence of a well-defined intermediate regime where the bosons are strongly dressed but the fermions are only weakly renormalized is formally justified if we take the limit of large N, where N is the number of fermion flavors.

Finally, it is possible that near the critical point, the system becomes unstable to the formation of some kind of ordered state (different from the primary order that onsets at the QCP). In the presence of time reversal or inversion symmetry, it is natural to expect a SC instability—the order parameter fluctuations induce an effective attractive interaction between the fermions, which is enhanced upon approach to the critical point (78–83). However, the strong scattering of the fermions off the fluctuations causes them to lose their coherence; the resulting SC T_c is determined by the competition between these two effects. For weak coupling, and sufficiently far away from the nematic QCP, superconductivity is enhanced in all symmetry channels (84, 85). At the QCP, and for sufficiently small λ, one can estimate the SC susceptibility in the regime, $\Omega_{\rm NFL} \ll T \ll \Omega_b$, by solving the Eliashberg equation for the SC vertex using the form Equation 5 for the bosonic self-energy (but ignoring the fermionic self-energy, which is small in this regime). For the Ising-nematic case, this predicts the SC susceptibility to diverge at a scale of

$$T_{c,\rm QCP} \sim \frac{\lambda^4}{E_F} \sim \Omega_{\rm NFL}. \qquad 9.$$

Thus, there is no parametric separation between the non-Fermi liquid and the SC scales, and both of these effects have to be taken into account on equal footing.

Other types of secondary-order parameters have been considered. Close to a ferromagnetic QCP in $d = 2$, an instability toward incommensurate spin order was proposed (86). Near an SDW transition, instabilities toward charge-density wave (CDW) (52, 57, 81) or pair-density wave (PDW) (87) orders were suggested to occur.

In summary, despite the valuable information provided by the perturbative treatments, there is still uncertainty about the basic properties of metallic QCPs. Clearly, a nonperturbative, controlled solution is highly desirable. In this review, we examine recent advances in numerical QMC simulations of metallic QCPs, describe the picture that emerges from the existing results, and point to some future directions and outstanding puzzles.

3. LATTICE MODELS AND QUANTUM MONTE CARLO TECHNIQUE

Arguably the most powerful numerical approach for solving quantum many-body problems is the QMC technique (88), which, despite an exponentially growing Hilbert space, allows us to sample the expectation values of arbitrary observables with polynomial effort in system size and inverse temperature. Typically, the problem is formulated as a path integral, mapping it to an effective $(d + 1)$-dimensional classical problem with Euclidean time playing the role of an additional dimension. The classical problem is then simulated using the traditional Monte Carlo method (89). Unfortunately, however, for generic models, the Boltzmann weight of the effective classical problem can turn out negative (or complex). In general terms, this is because the weights of the $(d + 1)$-dimensional system still represent quantum amplitudes rather than classical probabilities. In the present context, the occurrence of negative weights can in fact be traced back to the sign that arises in fermionic exchange statistics (90). Models that suffer from this problem can still be simulated using QMC techniques, but the computational complexity now grows exponentially with the system size and inverse temperature, thus obliterating the core advantage of the Monte Carlo approach. This is the famous sign problem (75).

Fortunately, as we elaborate below, many models of metallic QCPs can be formulated without a sign problem. Over the past several years, considerable progress has been made in establishing symmetry criteria for sign-free problems (91–97). In particular, the presence of antiunitary symmetries of the action matrix play a crucial role (92, 98, 99). For the models of metallic QCPs at hand, such an antiunitary symmetry is present and enables a sign-problem-free formulation. This

opens the way to large-scale, numerically exact simulations of these systems. In this section, we describe lattice models that realize metallic QCPs and the specific conditions for the lack of a sign problem, and we discuss some merits and limitations of the applied numerical technique.

3.1. Ising-Nematic Quantum Critical Point

In order to perform QMC simulations, we first need to formulate the problem on a discrete lattice. The microscopic model is then designed such that it realizes a quantum phase transition in the presence of itinerant electrons. To the degree that universality holds, the properties of this transition are independent of the particular lattice realization.

An Ising-nematic transition in a metal was studied using QMC in References 65 and 69. To do so, these works introduced a microscopic model containing two sets of degrees of freedom: fermions hopping on a two-dimensional square lattice and pseudospins that reside on the bonds. The Hamiltonian is given by

$$H_{\rm nem} = H_{\rm c} + H_{\rm nem} + H_{\rm int}, \qquad 10.$$

where

$$\begin{aligned} H_{\rm c} &= \sum_{\mathbf{r},\mathbf{r}',\sigma} [-t_{\mathbf{r},\mathbf{r}'} - \mu\delta_{\mathbf{r},\mathbf{r}'}] c^\dagger_{\mathbf{r}\sigma} c_{\mathbf{r}'\sigma}, \\ H_{\rm nem} &= -h \sum_{\langle \mathbf{r},\mathbf{r}'\rangle} \mu^x_{\mathbf{r},\mathbf{r}'} + V \sum_{\{\mathbf{r},\mathbf{r}'\},\{\mathbf{r}',\mathbf{r}''\}} \mu^z_{\mathbf{r},\mathbf{r}'} \mu^z_{\mathbf{r}',\mathbf{r}''}, \\ H_{\rm int} &= \alpha t \sum_{\langle \mathbf{r},\mathbf{r}'\rangle,\sigma} \mu^z_{\mathbf{r},\mathbf{r}'} \left(c^\dagger_{\mathbf{r}\sigma} c_{\mathbf{r}'\sigma} + h.c. \right). \end{aligned} \qquad 11.$$

Here, $c^\dagger_{\mathbf{r},\sigma=\uparrow,\downarrow}$ are fermion creation operators, $t_{\mathbf{r},\mathbf{r}'}$ are the hopping matrix elements, μ is the chemical potential, $\mu^{x,y,z}_{\mathbf{r},\mathbf{r}'}$ are Pauli matrices that act on the pseudospin degree of freedom at the bond connecting sites $\mathbf{r}$ and $\mathbf{r}'$, h is a "transverse field" that controls the quantum fluctuations of the pseudospins, and $V > 0$ is the strength of an antiferromagnetic interaction between the nearest-neighbor bonds $\{\mathbf{r},\mathbf{r}'\}$ and $\{\mathbf{r}',\mathbf{r}''\}$. The strength of the fermion-pseudospin coupling is set by α. In the disordered phase, where $\langle \mu^z_{\mathbf{r},\mathbf{r}\pm\hat{x}}\rangle = \langle \mu^z_{\mathbf{r},\mathbf{r}\pm\hat{y}}\rangle$, the system is symmetric under a C_4 rotation by $\pi/2$. For sufficiently small h, there is a transition into a phase in which the values of $\langle \mu^z_{\mathbf{r},\mathbf{r}'}\rangle$ on horizontal and vertical bonds become different. This phase spontaneously breaks the lattice rotational symmetry down to C_2. In this nematic phase, the dispersions of the fermions in the x and y directions are different.

To set up the model (Equation 10) for a QMC treatment (100, 101), the partition function is written as a discrete-time Euclidean path integral.[5] For each space-time configuration of the pseudospins, the fermions can be integrated out exactly, because their action is quadratic. The fermionic contribution to the Boltzmann weight is written as a product of two fermion determinants, $\det(M_\uparrow) \times \det(M_\downarrow)$, where $M_\uparrow$ and $M_\downarrow$ are the action matrices for spin up and down electrons, respectively. Crucially, $M_\uparrow = M_\downarrow$ and both matrices are real. Therefore, the effective bosonic action is real and nonnegative, and hence it is amenable to QMC simulations without suffering from the sign problem.

3.2. Spin-Density Wave Quantum Critical Point

In the case of a magnetic transition, we are not as fortunate; the magnetic order parameter couples differently to spin up and spin down fermions, and hence integrating out the fermions generally

[5]The results described here are independent of the size of the time step chosen.

does not produce a real, nonnegative Boltzmann weight. Nevertheless, one can formulate a lattice model that realizes a metallic SDW transition and is free of the sign problem.

In field theoretic treatments of an SDW metallic transition, one usually focuses on the vicinity of the hot spots, which are pairs of points on the Fermi surface connected by the magnetic ordering wavevector **Q**. It is generally believed that any universal properties of the transition are captured within a model that includes only a set of patches of the Fermi surface near the hot spots. One therefore has the freedom to deform the Fermi surface away from the hot spots without qualitatively changing the behavior near the QCP. Let us consider a model with two fermionic flavors, c_1 and c_2, with different dispersions, such that **Q** connects points on the Fermi surface of band 1 to points on band 2 but does not connect two points on the Fermi surface of the same band (see **Figure 1*c***). Then, to capture the coupling of the fermions to the SDW fluctuations near the hot spots, it is enough to consider only the part of the fermion-boson interaction of the form $\vec{\phi} \cdot (c_1^\dagger \vec{\sigma} c_2 + h.c.)$. The action, regularized on a lattice, then has the following form:

$$S_{\rm SDW} = S_{\rm c} + S_\phi + S_{\rm int}, \qquad 12.$$

where

$$S_{\rm c} = \sum_{\mathbf{k},\alpha=1,2,\sigma} \int d\tau \, c^\dagger_{\mathbf{k},\alpha,\sigma} \left(\partial_\tau + \varepsilon_{\alpha,\mathbf{k}}\right) c_{\mathbf{k},\alpha,\sigma},$$

$$S_{\rm int} = \sum_{\mathbf{r}} \int d\tau \, e^{i\mathbf{Q}\cdot\mathbf{r}} \vec{\phi}_{\mathbf{r}} \cdot c^\dagger_{\mathbf{r},1} \vec{\sigma} c_{\mathbf{r},2} + h.c., \qquad 13.$$

and S_ϕ is a lattice version of the bosonic part of the action in Equation 2, and $c^\dagger_{\mathbf{r},\alpha} = (c^\dagger_{\mathbf{r},\alpha,\uparrow}, c^\dagger_{\mathbf{r},\alpha,\downarrow})$. The order parameter $\vec{\phi}_{\mathbf{r}}$ can be either a one-, two-, or three-component vector, corresponding to an easy-axis, easy-plane, or isotropic magnetic order parameter.

The effective bosonic action obtained by integrating out the fermions in Equation 12 is real and positive semidefinite, and therefore the model is sign-problem free (64). This is because for every configuration of $\vec{\phi}_{\mathbf{r}}(\tau)$, the fermion action matrix is symmetric under an antiunitary transformation $\tilde{\mathcal{T}} = i\sigma_y \mathcal{K} U$, where $\mathcal{K}$ denotes complex conjugation, and U is a unitary transformation that changes $c_1 \to c_1$ and $c_2 \to -c_2$. Note that $\tilde{\mathcal{T}}^2 = -1$. The existence of such an antiunitary symmetry is a sufficient condition for the lack of a sign problem (92, 98, 99).

3.3. Determinant Quantum Monte Carlo Technique

We treat the models of Equations 10 and 12 using the standard determinant QMC method (102). Even in the absence of a sign problem, the method is computationally costly: Its complexity scales as $\beta \mathcal{N}^3$, where $\beta = 1/T$, and $\mathcal{N}$ is the number of lattice sites. Nevertheless, one can straightforwardly get to system sizes of 24×24 for the nematic case and 16×16 for the SDW case,[6] and temperatures as low as $T = 0.025$ in units of the hopping (about 1% of the Fermi energy). Fortunately, these system sizes and temperatures are sufficient to extract much of the physics of the QCP in both cases.

The details of the numerical implementations have been described in References 65 and 67. A few technical tricks turned out to be crucial to improve the convergence of the algorithm: First, global updates and parallel tempering schemes need to be introduced in the vicinity of the QCP to overcome critical slowing down. Second, convergence to the thermodynamic limit is dramatically

[6]The reason for the difference in the maximum accessible L between the nematic and the SDW models is that in the nematic model there is only one fermionic orbital per site, whereas in the SDW case there are two orbitals.

accelerated by simulating systems with a small orbital magnetic field that corresponds to a single flux quantum (103). The magnetic field is opposite for spin up and spin down fermions such that it does not introduce a sign problem. Recently, several new directions have been proposed to speed up QMC simulations that may allow access to larger system sizes (104–107).

Once converged, the simulations give numerically exact results, in the sense that they are devoid of any bias—free of systematic errors—and have statistical errors that can be made arbitrarily small by running the simulations longer. Thus, thermodynamic properties (such as the order parameter susceptibility) and imaginary-time correlation functions (such as the fermion Matsubara Green's function) can be calculated to any desired precision. Unfortunately, because the simulations are performed in imaginary time, one cannot directly access any real-time correlation functions. Computing real-time (or real-frequency) quantities requires an analytic continuation of the imaginary time data, which is a numerically unstable process and requires nontrivial additional assumptions. However, much insight into the physics can be gained by analyzing imaginary-time correlation functions directly, as we highlight below.

4. RESULTS

4.1. Phase Diagrams

We now review the results of the QMC simulations for the models describing a nematic (Equation 10; 67, 69) or easy-plane SDW (Equation 12; 65, 68) transition in a metal. The phase diagrams, shown in **Figure 2**, are qualitatively similar: Upon increasing the tuning parameter, the ordering temperature[7] (either nematic or SDW) decreases, extrapolating to zero at a quantum phase

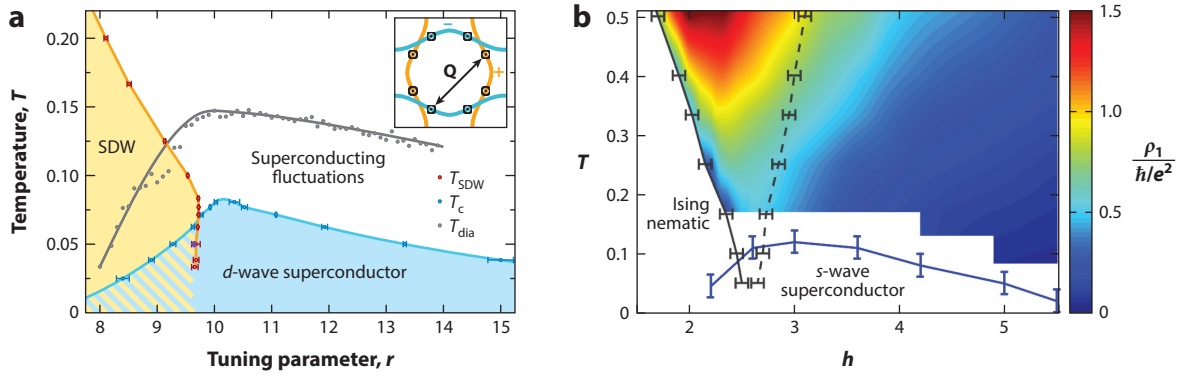

Figure 2

(*a*) Phase diagram of an easy-plane SDW model, with a fixed value of the Yukawa coupling, $\lambda = 3$. The shaded area marks coexistence between superconductivity and SDW order. The gray line marks the onsets of diamagnetism above T_c (defined as the change of sign of the magnetic susceptibility from paramagnetic to diamagnetic). The inset shows the structure of the superconducting order parameter in $\mathbf{k}$ space. $\mathbf{Q} = (\pi, \pi)$ is the magnetic ordering vector. (*b*) Phase diagram of the nematic model, as a function of the tuning parameter h and temperature T. The dashed lines indicate the value of h where the nematic susceptibility is half of its value at $h = h_c$ and the same temperature. The color scale shows a proxy ρ_1 to the DC resistivity (see Section 4.4). The following parameters were used: $\alpha = 1.5$, $V = 0.5t$, and $\mu = t$. Abbreviation: SDW, spin-density wave. Panel *a* adapted from Reference 65, and panel *b* adapted from Reference 69.

[7]In the SDW case, the thermal transition has Berezinskii–Kosterlitz–Thouless character, because the order parameter has XY symmetry.

transition. In the nematic case, the finite-temperature transition is continuous down to the lowest temperature displayed.[8] In the SDW case, there is some evidence that the transition becomes very weakly first order at the lowest temperature, $T \sim 0.025$, accessible in the numerics.[9] (All energy scales are in units of the hopping matrix element of the fermions on the lattice.) In both cases, the putative QCP is covered by a SC phase (detected by measuring either the SC susceptibility or the superfluid stiffness), with a maximum T_c occurring near (or slightly to the disordered side of) the QCP. The symmetry of the SC order parameter is *s* wave in the nematic case, whereas in the SDW case it is *d* wave. For the SDW problem, a regime of substantial SC fluctuations between T_c and $\sim 2T_c$ is reported in Reference 65, as manifested by a reduction of the single-particle density of states and an enhanced diamagnetic susceptibility.

It is interesting to ask what features of the models control the maximum T_c. In the SDW case, this question has been addressed in some detail (68, 71). For a fixed band structure, the overall phase diagram evolves smoothly with the strength of the Yukawa coupling λ, with the maximum SC T_c being initially proportional to λ^2; at larger λ, T_c saturates to a value of about $0.04E_F$. T_c near the nematic QCP has not been studied at the same level of detail but seems to behave similarly. Preliminary simulations (108) show that T_c in the isotropic [$O(3)$-symmetric] SDW case has similar trends. In the planar SDW problem, the maximal T_c was found to be strongly dependent on the angle at which the Fermi surfaces meet at the hot spot (71): Over some range of the angle θ_{hs} and λ, $T_c \propto \sin(\theta_{hs})$. At larger values of λ, T_c seems to be less dependent on θ_{hs}.

In both the Ising-nematic and the planar SDW case, the QCP is inside the SC phase. Because the Fermi surface is fully gapped in the SC phase in both cases,[10] we expect the QCP to be of the $d = 2 + 1$ Ising or XY types, respectively. Hence, strictly speaking, a pristine metallic QCP does not exist in either case. A metallic QCP may be stabilized by breaking both time-reversal and inversion symmetries or by applying a magnetic field. However, in our numerical QMC simulations, doing so would immediately introduce a sign problem, and this option has not been explored. A model undergoing an Ising ferromagnetic transition (72) has shown no superconductivity down to the lowest temperatures considered. However, as the Yukawa coupling is increased, the SC correlations grow rapidly, indicating that the ground state is probably SC.

Finally, besides the primary order parameter (either planar SDW or nematic) and superconductivity, we do not find any substantially enhanced fluctuations of any other form of order anywhere in the phase diagram. Specifically, we have computed CDW and PDW correlations. The SC susceptibility is always peaked at $\mathbf{Q} = 0$, with no secondary peaks at nonzero $\mathbf{Q}$, indicating no proximate PDW instability. The CDW susceptibility is very moderately enhanced upon approaching the SDW QCP and then strongly suppressed upon entering the SC phase. If particle–hole symmetry is present, the SDW model has an increased symmetry that relates the SC and CDW order parameters, and the susceptibilities of the two order parameters are identical (52, 81). However, a recent QMC study found that even a small breaking of particle–hole symmetry strongly lifts the degeneracy between the two types of order in favor of superconductivity (70).

4.2. Order Parameter Correlations

Next, we examine the correlations of the order parameter near the QCP. We focus on the metallic regime above T_c.

[8] At smaller fermionic densities (not shown) the nematic transition may turn weakly first order.

[9] Simulations at $T = 0$ are possible; however, to the best of our knowledge, none have been performed to date for the easy-plane case.

[10] Note that the SC state in the SDW case possesses a nodeless *d*-wave order parameter, having an opposite sign on the two portions of Fermi surface that are related to each other by $\pi/2$ rotation. See the inset of **Figure 2**.

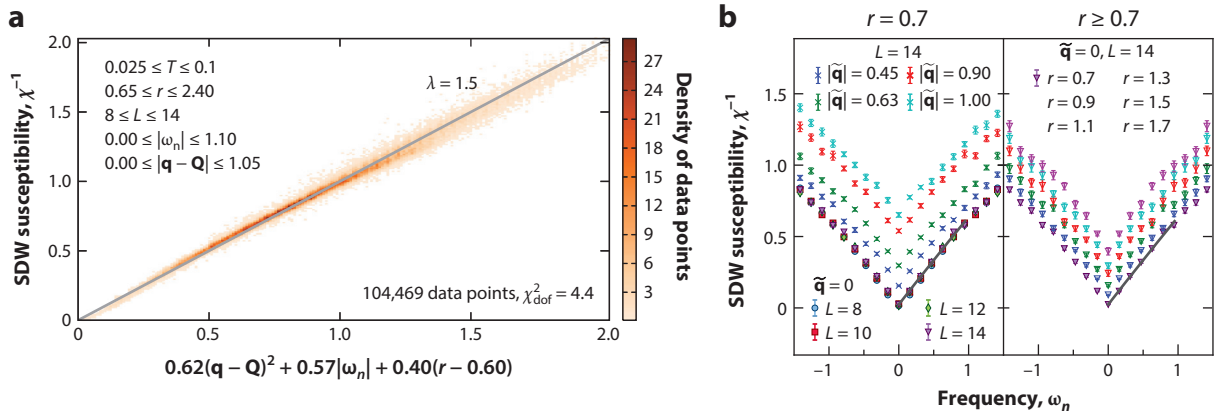

Figure 3

(*a*) The inverse SDW susceptibility, χ^{-1}, near the quantum critical point for different values of L, T, $\mathbf{q} - \mathbf{Q}$, ω_n, and r. The horizontal axis is the functional form χ^{-1}_{fit}. The color indicates the density of data points for this value of χ_{fit}. (*b*) A slice through the same data as in panel *a*, showing χ^{-1} versus ω_n for different values of $\tilde{\mathbf{q}} = \mathbf{q} - \mathbf{Q}$ and r. In both panels, $\lambda = 1.5$ and $T = 0.025$. Panel *a* adapted from Reference 14.

Figure 3 shows the susceptibility, χ, of the planar SDW order parameter as a function of temperature, tuning parameter, frequency, momentum, and system size. The value of the Yukawa coupling, $\lambda = 1.5$, was chosen such that the lowest temperature displayed, $T = 0.025$, is just above the SC T_c. **Figure 3*a*** shows that χ^{-1} can be remarkably well approximated by a simple functional form over the entire regime: $\chi^{-1} \approx \chi^{-1}_{\text{fit}}$, where

$$\chi^{-1}_{\text{fit}} = a|\mathbf{q} - \mathbf{Q}|^2 + b|\omega_n| + c(r - r_c). \quad 14.$$

The values of a, b, c, and r_c are shown in **Figure 3*a***. **Figure 3*b*** shows the dependence of χ^{-1} on ω_n for different values of $\mathbf{q}$ and r at $T = 0.025$. For other values of λ, χ is similarly well described by χ^{-1}_{fit}.

Equation 14 is precisely the form we expect from naïvely integrating out the fermions and treating the resulting effective action at the Gaussian level, à la Hertz–Millis theory (24, 26). There is one notable difference, however: This treatment (26) gives that the thermal mass (i.e., a temperature-dependent additive constant to Equation 14) should scale as $T \log(1/T)$. However, in Equation 14, we did not include a thermal mass term at all, because it hardly affects the quality of the fit within this resolution. A more careful analysis (68) shows that the thermal mass term is nearly quadratic in T for $T < 0.3$ and nearly linear at higher temperatures.

Next, we turn to the order parameter susceptibility near the nematic QCP. We first focus on a moderately small value of the Yukawa coupling, $\alpha = 0.5$ in Equation 10. The static correlations, $D^{-1}(\omega_n = 0)$, are well described (65) by a simple Curie–Weiss form:

$$\tilde{D}^{-1} = A[T + b|\mathbf{q}|^2 + c(h - h_c)]. \quad 15.$$

The dynamical correlations turn out to be more intricate and do not permit such a simple description. **Figure 4*a*** shows the inverse bosonic propagator D^{-1} as a function of Matsubara frequency for different values of $\mathbf{q}$ near the QCP. $D^{-1}(\omega_n, \mathbf{q} = 0)$ is markedly different from $D^{-1}(\omega_n, \mathbf{q} \neq 0)$, as one may expect for a $\mathbf{q} = 0$ order parameter from Hertz theory (24). $D^{-1}(\omega_n, \mathbf{q} \neq 0)$ has an apparent "cusp" at $\omega_n = 0$, as expected for a bosonic mode Landau damped by the fermions. However, we could not fit D^{-1} to a simple scaling form. As seen in the inset of **Figure 4*a***, the slope of D^{-1} near $\mathbf{q} = 0$ increases with decreasing $|\mathbf{q}|$. The q dependence of this slope is in the

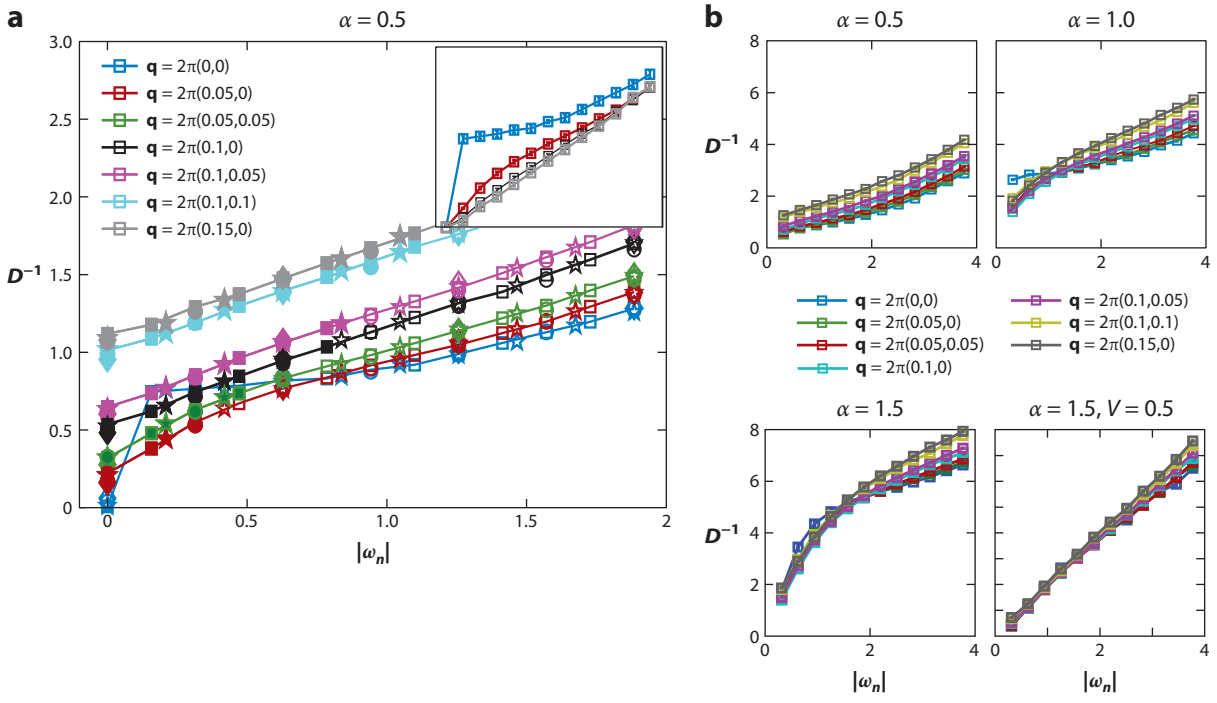

Figure 4

The inverse bosonic susceptibility, D^{-1} near the nematic quantum critical point for different values of the Yukawa coupling α (Equation 10). (*a*) D^{-1} versus ω_n for $\alpha = 0.5$ and different values of $\mathbf{q}$. Here, $h \approx h_c$, and different symbols represent different temperatures: squares, stars, circles, and diamonds correspond to $T = 0.025$, 0.033, 0.05, and 0.1, respectively. Solid (open) symbols correspond to points where $v_F|\mathbf{q}| \geq \omega_n$ ($v_F|\mathbf{q}| < \omega_n$), where v_F is the minimal value of the bare Fermi velocity on the Fermi surface. (*Inset*) the same data with the value of $D^{-1}(\omega_n = 0)$ subtracted. (*b*) D^{-1} versus ω_n for different values of α at $h \approx h_c$ and $\beta = 20$. In all the simulations, $V = 1$ and $\mu = -0.5$, except in the lower right panel of panel *b*), where $V = 0.5$ and $\mu = -1$. The results are for systems of size $L = 20$. Panel *a* adapted from Reference 65.

same direction as predicted by $|\omega_n|/|\mathbf{q}|$ Landau damping term, but it is much weaker. This may be due to finite size and finite temperature effects (109, 110). A qualitatively similar behavior was found near an Ising ferromagnetic transition (72), where the ferromagnetic propagator was fit to a modified Hertz–Millis form.

At larger values of the Yukawa coupling, D^{-1} shows qualitatively different behavior. The contrast between $D^{-1}(\omega_n = 0)$ and $D^{-1}(\omega_n \neq 0)$ becomes less pronounced as the Yukawa coupling increases. Most dramatically, for $\alpha = 1.5$, D^{-1} loses its $\mathbf{q}$ dependence almost completely; this is most pronounced when the value of the exchange coupling between the bosonic degrees of freedom is decreased from $V = 1$ to $V = 0.5$ (see **Figure 4*b***).

4.3. Single Fermion Properties

Near a metallic QCP, we expect the scattering of fermions off the order parameter fluctuations to lead to a breakdown of Fermi liquid behavior. We now address the single-particle properties upon approaching the SDW and Ising-nematic QCPs.

The imaginary time or Matsubara frequency properties can be computed directly from the QMC simulations. In addition, some information about the properties of the fermion spectral

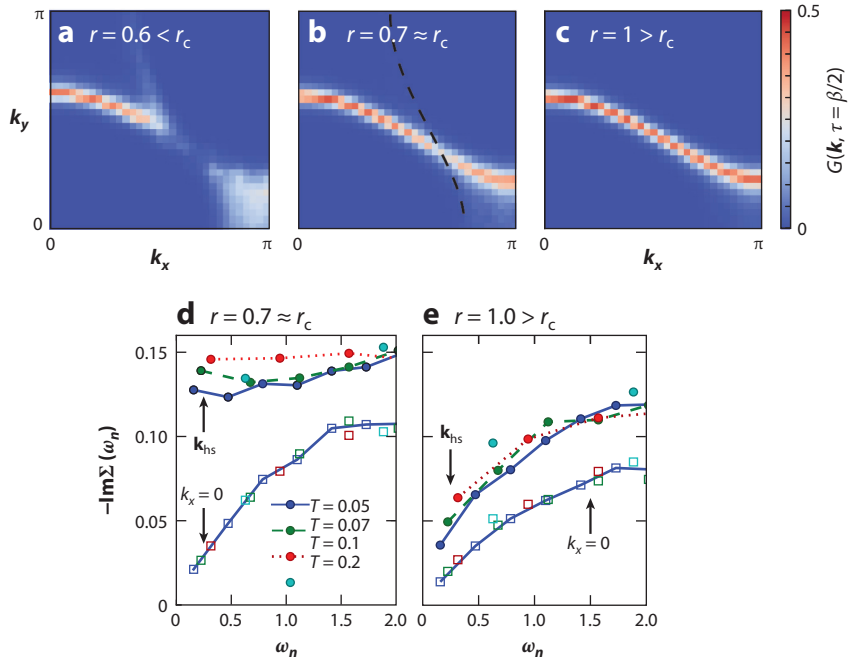

Figure 5

Single-particle properties near an SDW QCP with $\lambda = 1.5$. (*a–c*) The Green's function $G(\mathbf{k}, \tau = \beta/2)$ as a function of $\mathbf{k}$, for different values of the tuning parameter r. The Green's function is shown for one orbital only; the location of the Fermi surface of the other orbital is indicated by a black dashed line in panel *b*. (*d,e*) the imaginary part of the self-energy, $\mathrm{Im}\Sigma(\mathbf{k}_F, \omega_n)$, near the QCP (*d*) and away from it (*e*). The self-energy is shown at one of the hot spots ($\mathbf{k} = \mathbf{k}_{\mathrm{hs}}$) and at a Fermi surface point with $k_x = 0$, away from the hot spots. Abbreviations: QCP, quantum critical point; SDW, spin-density wave. Figure adapted from Reference 68.

function at real frequencies of the order of T can also be obtained. This is possible through the relation, valid for $0 < \tau < \beta$ (111),

$$G(\mathbf{k}, \tau) = \int d\omega \, \frac{e^{-\omega(\tau - \beta/2)}}{2\cosh(\beta\omega/2)} A(\mathbf{k}, \omega), \qquad 16.$$

where $A(\mathbf{k}, \omega)$ is the spectral function. From here, we see that $G(\mathbf{k}, \tau = \beta/2)$ gives the integrated spectral weight in a window of width $\sim T$ around the Fermi level. **Figure 5*a–c*** shows a colormap of this quantity versus $\mathbf{k}$ for one of the orbitals that forms the horizontal Fermi surface shown in **Figure 1*c*** for different values of the tuning parameter r approaching an SDW QCP (68). In the ordered state, $r < r_c$ (**Figure 5*a***), the reconstruction of the Fermi surface is clearly visible, and a gap opens at the hot spots. Near the QCP (**Figure 5*b***), the gap at the hot spots fills in, although $G(\mathbf{k}, \beta/2)$ is still significantly suppressed at the hot spots compared with other regions of the Fermi surface. Finally, away from the QCP (**Figure 5*c***), a full Fermi surface is recovered.

Next, we examine the fermion self-energy, $\Sigma(\mathbf{k}, \omega_n)$, at different points on the Fermi surface. The imaginary part of $\Sigma(\mathbf{k}, \omega_n)$ is shown at the intersection of the Fermi surface and the y axis (which is far away from the hot spots) and at the hot spot ($\mathbf{k}_{\mathrm{hs}}$), either near the QCP or away from the QCP (**Figure 5*d,e***, respectively). Away from the hot spots, $\Sigma(\mathbf{k}, \omega_n)$ tends linearly toward zero, which is consistent with Fermi liquid behavior. At the hot spots, the self-energy is larger than it is away from the hot spots; this is particularly pronounced in the vicinity of the QCP, where

$\Sigma(\mathbf{k}_{\rm hs}, \omega_n)$ is nearly frequency and temperature independent. This marks a strong deviation from Fermi liquid behavior at the hot spots.

The near independence of the self-energy of ω_n and T is surprising; most field-theoretical models predict $\Sigma(\omega_n) \sim i\,\mathrm{sgn}(\omega_n)\sqrt{|\omega_n|}$ at the hot spots. It is not clear whether the behavior found in the simulations represents a true asymptotic property of the QCP. The lowest temperature in the simulations is intrinsically limited by the SC transition ($T_c \approx 0.025$ for $\lambda = 1.5$). Note that for all but the smallest temperature and frequency, $T = 0.05$ and $\omega_n = \pi/T$, the self-energy is smaller in magnitude than ω_n, and we can then identify a non-Fermi liquid scale $\Omega_{\rm NFL} \sim 0.05 \approx 2T_c$. Thus, there is no separation of scales between non-Fermi liquid behavior and superconductivity.

Next, we describe the single-fermion properties in the nematic case. **Figure 6*a–d*** shows a colormap of $G(\mathbf{k}, \beta/2)$ for different parameters. In the noninteracting case ($\alpha = 0$), this function is strongly peaked at the Fermi surface. In the presence of interactions ($\alpha = 1.5$, $V = 0.5$) but away from the QCP ($h = 5.5$), a clear Fermi surface is still present, although some broadening is visible near the hot regions around $\mathbf{k} = (\pi, 0)$ and $(0, \pi)$. In the vicinity of the QCP ($h = 2.8 \approx 1.1h_c$), a dramatic reorganization of the low-energy spectral weight occurs. Although the Fermi surface near the cold spots along the diagonal remains reasonably well defined (even though it is substantially broadened), the Fermi surface in the hot regions is almost completely washed out, with spectral weight distributed over a broad momentum range.

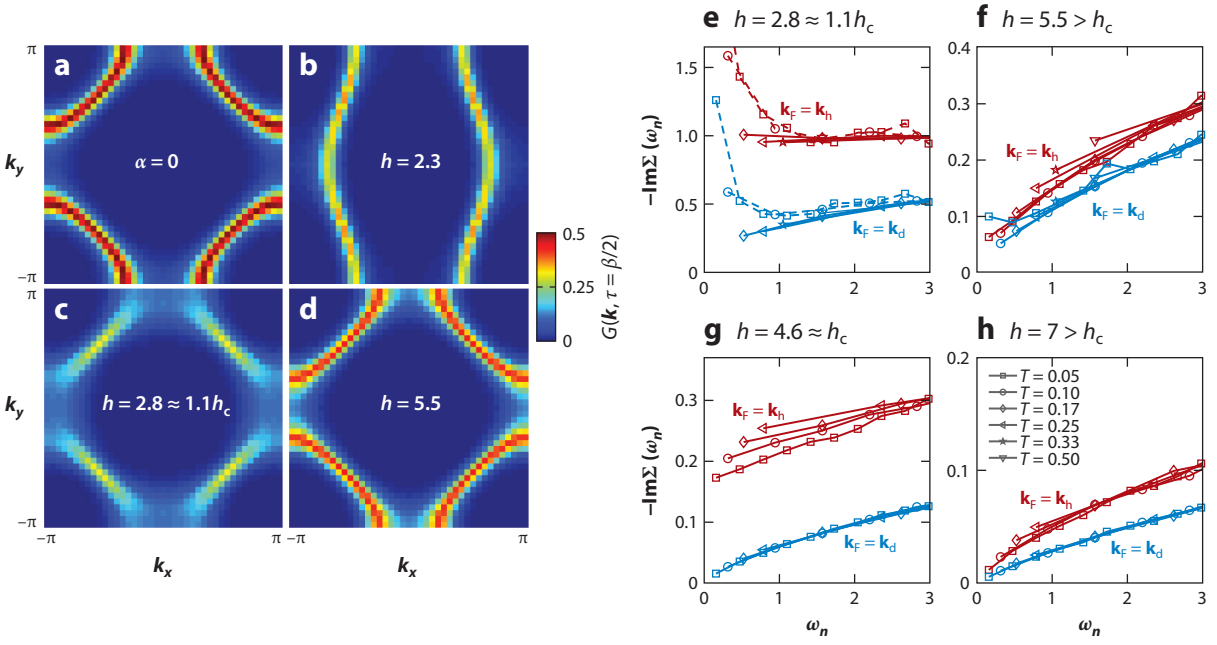

Figure 6

Single-fermion properties near a nematic quantum critical point. (*a*) The imaginary time Green's function $G(\mathbf{k}, \tau = \beta/2)$ as a function of $\mathbf{k}$ for noninteracting electrons ($\alpha = 0$) and temperature $T = 0.17$. (*b–d*) $G(\mathbf{k}, \tau = \beta/2)$ for an interacting system with $\alpha = 1.5$, $V = 0.5$, $\mu = 1$, and $T = 0.17$ for different values of the tuning parameter, h. In panel *b*, the system is in the nematic phase; a small symmetry-breaking field was applied in order to pin one of the two configurations of the order parameter. (*e,f*) Imaginary part of the Matsubara self-energy at the Fermi surface, $-\mathrm{Im}\mathbf{k}_F$, $\Sigma(\mathbf{k}, \omega)$ for two values of h, for the same parameters as in panels (*b–d*). The self-energy is shown at the cold spot on the diagonal, $\mathbf{k}_F = \mathbf{k}_d \parallel (1, 1)$, and at a point in the hot region, k_h, which is the intersection of the Fermi surface with the segment from $(0, \pi)$ to (π, π). Similar data are shown in panels (*g,h*) for a weaker coupling system with $\alpha = 1.0$, $V = 1.0$, and $\mu = 0.5$.

This dichotomy between the cold spots and the hot regions is also apparent in the behavior of the fermionic self-energy, shown in **Figure 6*e–h***. **Figure 6*e,f*** shows $\mathrm{Im}\Sigma(\mathbf{k}_\mathrm{F}, \omega_n)$ for the parameters used in **Figure 6*a*** ($\alpha = 1.5$, $V = 0.5$, and $\mu = 1$); **Figure 6*g,h*** shows the same quantity for a smaller value of the Yukawa coupling, $\alpha = 1$, $V = 1$, and $\mu = 0.5$. Away from the QCP, both $\mathrm{Im}\Sigma(\mathbf{k}, \omega_n)$ in the hot region [$\mathbf{k} = \mathbf{k}_\mathrm{h}$, which is along the line from $(0, \pi)$ to (π, π)] and at the cold spot ($\mathbf{k} = \mathbf{k}_\mathrm{d}$, along the diagonal) depend approximately linearly on ω_n.[11] In contrast, near the QCP, $\mathrm{Im}\Sigma(\omega_n)$ in the hot regions is much larger and does not seem to vanish as $\omega_n \to 0$ and $T \to 0$. The strong upturn of $\mathrm{Im}\Sigma(\omega_n)$ at low frequencies in **Figure 6*e*** is due to the onset of a SC gap.[12] At higher frequencies, $\mathrm{Im}\Sigma(\mathbf{k}_\mathrm{h}, \omega_n)$ in **Figure 6*e*** is strikingly frequency and temperature independent, which is reminiscent of the behavior found in the SDW case at the hot spot (**Figure 5*d***). Note that in the stronger coupling simulation of **Figure 6*e***, $\mathrm{Im}\Sigma(\mathbf{k}_d, \omega_n)$ has a substantial $\omega_n \to 0$ extrapolation even at the cold spot; in contrast, in **Figure 6*g*** it seems to extrapolate to zero.

Thus, in both the SDW and nematic QCPs, strong deviations from Fermi liquid behavior are found at temperatures $T \geq T_\mathrm{c}$, at least in some regions of the Fermi surface. The character of these non-Fermi liquid regimes are different from those predicted by theories of metallic criticality; in particular, the self-energy found in the numerical simulations is much less temperature and frequency dependent than expected. The non-Fermi liquid regimes terminate at $T = T_\mathrm{c}$, where a gap opens on the entire Fermi surface.

4.4. Transport

The frequency-dependent conductivity near a metallic QCP is of particular interest. Unfortunately, computing this quantity from QMC techniques is a highly nontrivial task. Because all dynamical properties are defined in real frequency, they are not easily accessible in QMC simulations performed in imaginary time. In principle, there is a one-to-one correspondence between the correlation functions in real and imaginary times. However, such an analytical continuation involves inverting a nearly singular matrix (with exponentially small eigenvalues). Hence, any uncertainty in the QMC data (inevitably present because of statistical errors) gets strongly amplified when one attempts to convert the data into real time.

The reverse procedure, of going from real-time spectral functions to imaginary-time correlations, does not suffer from this problem. Therefore, the QMC data can be used to constrain the behavior of the real-time spectral functions but cannot determine them uniquely. If additional assumptions are made, one can extract model spectral functions that are consistent with the data. For example, the maximum entropy method (112) attempts to find the least structured spectral function that can reproduce the imaginary-time data.

Below, we describe the results for the imaginary-time current–current correlation function and several methods that were used to analyze this data and extract information about the real-time optical conductivity, $\sigma(\omega)$. The analysis is similar to the maximum entropy method and gives similar results; however, it makes the physical assumptions more explicit.

The Matsubara frequency current–current correlation function $\Lambda(\omega_n)$ is related to the real part of the optical conductivity by

$$\Lambda(\omega_n) = \int \frac{d\omega}{\pi} \frac{\omega^2 \sigma(\omega)}{\omega_n^2 + \omega^2}. \qquad 17.$$

[11] The small nonzero extrapolation of $\mathrm{Im}\Sigma(\omega_n)$ to $\omega_n = 0$ in **Figure 6*f*** is likely to be a finite temperature effect; it decreases with decreasing temperature.

[12] Compare this behavior to that of the self-energy in the SC state within BCS theory, $\Sigma_\mathrm{BCS}(\mathbf{k}_\mathrm{F}, \omega_n) \sim |\Delta|^2/(i\omega_n)$, where Δ is the gap.

The QMC data for $\Lambda(\omega_n)$ was found to be well described by the following simple ansatz (69):

$$\Lambda_{\rm fit}(\omega_n) = \sum_{j=1}^{n} \frac{A_j}{\omega_n^2 + \gamma_j|\omega_n| + \Omega_j^2}\,. \qquad 18.$$

Here, n is the number of Lorentz oscillator components, and A_j, Ω_j, and γ_j ($j = 1,\ldots,n$) are fitting parameters. Analytically continuing this to real frequency, we get the corresponding real part of the conductivity:

$$\sigma_{\rm fit}(\omega) = \sum_{j=1}^{n} \frac{A_j\gamma_j}{(\Omega_j^2 - \omega^2)^2 + \gamma_j^2\omega^2}. \qquad 19.$$

It turns out that the minimal number of components required to obtain a good fit to the QMC data is $n = 2$: Essentially, $\sigma(\omega)$ is composed of a strongly temperature-dependent Drude-like peak and a broad, weakly temperature-dependent background. This procedure yields a proxy for the DC resistivity, $\rho_1 = 1/\sigma_{\rm fit}(\omega = 0)$. A more conventional maximum entropy analysis yields qualitatively similar results (69). However, the resulting $\sigma(\omega)$ is not unique: Adding more components ($n > 2$) gives a fit with a similar quality. This is the main source of possible systematic errors in this analysis, as we discuss further below.

Another useful diagnostic of the low-frequency part of the optical conductivity is obtained by examining the current–current correlation function as a function of imaginary time. $\tilde{\Lambda}(\tau)$ is related to the conductivity via

$$\tilde{\Lambda}(\tau) = \int \frac{d\omega}{2\pi} \frac{\omega\cosh[\omega(\beta/2 - \tau)]}{\sinh(\omega\beta/2)}\sigma(\omega). \qquad 20.$$

Thus, we see that derivatives of $\tilde{\Lambda}(\tau)$ at $\tau = \beta/2$ can be interpreted as moments of $\sigma(\omega)$ weighted by a window function of width $\sim T$:

$$\left[\left(\frac{d}{d\tau}\right)^{2m} \tilde{\Lambda}(\tau)\right]_{\tau=\beta/2} = \int \frac{d\omega}{2\pi} \frac{\omega^{2m+1}}{\sinh(\omega\beta/2)}\sigma(\omega). \qquad 21.$$

If the low-frequency conductivity is characterized by a simple Drude-like peak, then Equation 21 can be used to extract information about its weight and its width. We define a second resistivity proxy in terms of the moments in Equation 21 as

$$\rho_2 = [(d^2\tilde{\Lambda}/d\tau^2)/(2\pi\tilde{\Lambda})^2]_{\tau=\beta/2}. \qquad 22.$$

If $\sigma(\omega)$ has a Lorentzian form with width much less than T, then ρ_2 asymptotically coincides with the DC resistivity as $T \to 0$. Furthermore, if $\sigma(\omega)$ has a single-peak structure at low frequency and the width of the peak scales as T^a with $a \leq 1$, then ρ_2 is proportional to the DC resistivity as $T \to 0$. Using ρ_2 as a diagnostic for $\sigma(\omega)$ has the advantage that it does not rely on any fitting procedure. However, it suffers from the same uncertainty as ρ_1: It is insensitive to fine structure in $\sigma(\omega)$ on a scale of $\omega \sim T$ or smaller. If such structure exists, then ρ_2 does not serve as a good indicator of the DC resistivity.

With these caveats in mind, **Figure 7** shows the analysis of the transport properties near the QCP, starting with the nematic model. The Matsubara frequency current–current correlation function, $\Lambda(\omega_n)$, near the nematic QCP is plotted in **Figure 7*a***. The results of the two-component fit (Equation 18) for different temperatures at $h \approx h_c$ are shown in **Figure 7*b***. As the temperature is lowered, the Drude-like component becomes narrower and higher, whereas its integrated weight is approximately constant. The corresponding proxy of the DC resistivity, $\rho_1 = 1/\sigma_{\rm fit}\,(\omega = 0)$, is shown versus temperature in **Figure 7*c,d***; it is also shown as a color map across the (h, T) phase diagram in **Figure 2*b***.

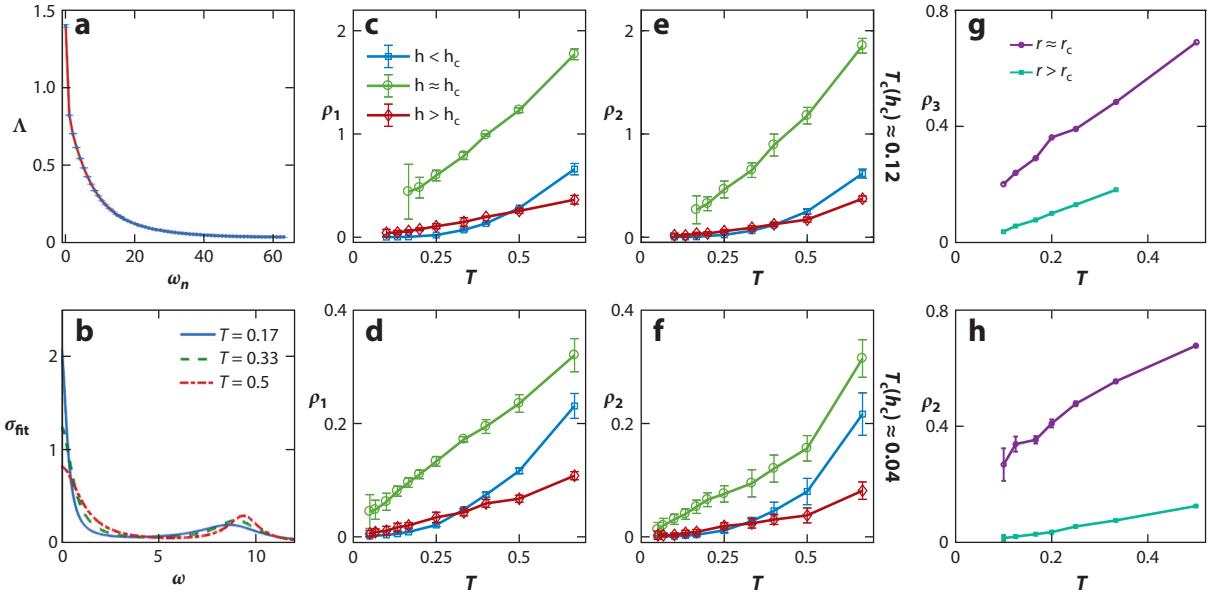

Figure 7

(*a*) Current–current correlator $\Lambda(\omega_n)$ near a nematic QCP. In this simulation, $T = 0.17$, $h \approx 2.6$, and the following parameters were used: $\alpha = 1.5$, $V = 0.5$, and $\mu = 1$. The red line shows a fit to Equation 18. (*b*) Fitted optical conductivity $\sigma_{\text{fit}}(\omega)$ (Equation 19) in units of $e^2/\hbar$ for three temperatures. (*c–f*) Temperature dependence of the resistivity proxies ρ_1 and ρ_2 (in units of $\hbar/e^2$) for parameters $\alpha = 1.5$, $V = 0.5$, and $\mu = 1$ [(*c*,*e*), for $h = 2.0 < h_c$, $h = 2.6 \approx h_c$, and $h = 5.5 > h_c$] and $\alpha = 1.0$, $V = 1.0$, and $\mu = 0.5$ [(*d*,*f*), for $h = 4.0 < h_c$, $h = 4.6 \approx h_c$, and $h = 7.0 > h_c$]. For $h < h_c$, a small symmetry-breaking field has been applied, such that the resistivity tensor is anisotropic. Only the smaller component of the resistivity proxy is shown. (*g*,*h*) Resistivity proxies versus T near an SDW QCP. Here, we set $\lambda = 3$, as in **Figure 2**. (*g*) The maximum entropy result ρ_3, and (*h*) the proxy ρ_2 shown near the QCP ($r = 10.2$) and deep in the disordered side ($r = 20$). Abbreviations: QCP, quantum critical point; SDW, spin-density wave. Figure adapted from Reference 69.

Figure 7*e*,*f* shows the temperature dependence of the proxy ρ_2. It is in qualitative agreement with ρ_1: Near $h = h_c$, both ρ_1 and ρ_2 are significantly larger than they are away from the QCP, and they depend nearly linearly on temperature, although for the larger coupling strength ($\alpha = 1.5$) the temperature range of this quasi-linear regime is small. The SC phase sets the lower limit on the temperatures we can access. In the strongly coupled case, the resistivity proxies become large at moderate temperatures, exceeding $\hbar/e^2$ at a temperature $T \approx 0.3t \sim 0.1E_F$.

Similar results are obtained in the SDW model. The data are consistent with an optical conductivity dominated by a Drude-like peak with a width of order $\sim T$ and a nearly constant weight. The maximum entropy analysis result, ρ_3, shown in **Figure 7*g***, is qualitatively consistent with the resistivity proxy ρ_2 shown in **Figure 7*b***. With the limited temperature range accessible to us, it is difficult to establish a power-law behavior for the temperature dependence of ρ_2 and ρ_3. If we assume a power-law behavior $\rho \sim T^x$ at low temperatures, we find $x > 1$ for $r > r_c$, and $x < 1$ for $r \approx r_c$.

5. CONCLUSIONS AND OUTLOOK

The first batch of QMC simulations of metallic QCPs described in this review has yielded remarkable and often unexpected insights and opened new questions for numerical and analytical investigation. In this concluding section, we review and interpret the principal conclusions of these studies and discuss their broader implications.

The most basic fact about both the SDW and Ising-nematic models is that in both cases, the thermal transitions remain continuous at least down to low temperatures ($T \lesssim 0.01 E_F$). Both models exhibit domes of high-temperature superconductivity near their putative QCPs, with a maximum T_c occurring near the QCP, confirming the notion that critical fluctuations are conducive to superconductivity. Notably, in both types of QCPs, superconductivity is the only contender other than the primary order parameter. Thus, the physics of competing orders, with many ordered phases in a delicate balance with each other, does not appear to be a ubiquitous feature of metallic QCPs. In addition, no pseudogap regime is found near the QCPs, in the sense that there is no broad regime characterized by a gap in the fermionic spectrum that is not associated with a nearby ordered phase (such as an SDW or a superconductor).

Consequently, these QCPs are not actually metallic, because they occur within SC phases. Though the models can in principle be supplemented by repulsive interactions and/or symmetry breaking (such as a magnetic field) to suppress superconductivity, the resulting sign problem drastically limits the accessible system sizes and temperatures.

Nonetheless, the sign-free models exhibit interesting phenomenology in the region of their quantum critical fans above T_c, much of which persists into the SC state, except at the lowest frequencies. We can thus operationally call this metallic quantum critical behavior.

Some of the robust characteristics of this quantum critical regime, common to both the SDW and Ising-nematic QCPs, include the following: (*a*) The order parameter correlations are strongly affected by the coupling to the fermions, and are consistent with overdamped dynamics of the bosons. (*b*) The single-particle fermionic correlator shows non-Fermi liquid behavior of an unexpected kind. Strikingly, the fermionic self-energy is nearly frequency and temperature independent over a broad regime above the SC T_c. (*c*) The transport properties show strong anomalies, which is consistent with a significant broadening of $\sigma(\omega)$ near the QCP. If the results are interpreted in terms of a single Drude-like peak, then the data are consistent with a large DC resistivity that is nearly linear in temperature.

The order parameter dynamics of the SDW model are in broad agreement with Hertz–Millis theory, with the exception of the temperature dependence of the order parameter susceptibility (the latter displays a crossover behavior from $1/T$ to $1/T^2$ upon decreasing temperature). The dynamical critical exponent is $z = 2$. In the Ising-nematic case, the static order parameter correlations are well described by a simple mean field–like form, again in agreement with Hertz–Millis theory. However, the order parameter dynamics do not admit such a simple description. Although it is qualitatively similar to the $|\omega_n|/|\mathbf{q}|$ form expected from Hertz–Millis theory at relatively weak values of the coupling, its form evolves substantially as the coupling strength is increased. At stronger couplings, the $\omega_n \neq 0$ propagator becomes increasingly momentum independent (i.e., the effective dynamical critical exponent increases). It is tempting to associate this behavior with an emergent local quantum criticality, although the present studies of the Ising-nematic model do not yet establish generic order parameter dynamics in the strong coupling regime.

The single fermion correlations in the quantum critical regime are simpler than the order parameter correlations but also more unexpected. At weaker coupling, the fermionic correlations are consistent with a renormalized Fermi liquid, whereas the order parameter correlations are substantially altered, which is consistent with the conclusions of Section 2.2. At stronger coupling, in both the SDW and Ising-nematic cases, there is a non-Fermi liquid regime above T_c.[13] This regime exhibits substantial loss of quasiparticle coherence in the hot regions of the Fermi surface:

[13] It remains to be seen whether the non-Fermi-liquid regime extends to temperatures parametrically higher than T_c in an appropriate limit.

the hot spots in the SDW case, and everywhere but the cold spots in the Ising-nematic case. At these momenta, the imaginary part of the self-energy is nearly constant, with only weak dependence on frequency and temperature. This violation of Fermi liquid behavior is stronger than predicted by field theoretical methods, which predict a power-law dependence of the self-energy on frequency.

The origin of this behavior has yet to be clarified. It may well be a characteristic of a finite-temperature crossover rather than being representative of the asymptotic infrared properties of any QCP. (Note, however, that this behavior extends down to temperatures close to T_c.) In our opinion, it is worth considering the more radical possibility that the metallic quantum critical ground state is in fact characterized by a nonzero $\mathrm{Im}(\Sigma)$ in the $\omega_n \to 0$ limit.

The transport signatures of the two models show unambiguously that the optical conductivity is strongly affected by the proximity of the QCP. The implications for the DC transport, however, merit both excitement and caution. The data in both models are consistent with T-linear resistivity near the QCP; however, this analysis is subject to the usual uncertainties associated with analytical continuation of imaginary time data. In particular, it relies heavily on the assumption that there is no structure in $\sigma(\omega)$ at frequencies much smaller than T. Developing ways of independently testing the consistency of this assumption within the simulations is desirable.

Future investigations of metallic QCPs will hopefully develop both the breadth and depth of our understanding. The robustness of the behavior described in this review should be tested by simulating microscopic models with different band structures and different kinds of broken symmetry. Further direct comparisons of the QMC data to perturbative analytical calculations, at least in the weak to intermediate coupling regimes, can provide useful insights into the interpretation of the results. Finally, sign-problem-free models, such as the ones often used to describe metallic QCPs, form a zero-measure set in Hamiltonian space. It is important to study to what extent the results presented here carry over in the presence of more generic interactions. Devising ways to do this numerically is, of course, a highly challenging problem at the frontier of the field of many-body quantum physics.

DISCLOSURE STATEMENT

The authors are not aware of any affiliations, memberships, funding, or financial holdings that might be perceived as affecting the objectivity of this review.

ACKNOWLEDGMENTS

It is a pleasure to thank C. Bauer, S. Chatterjee, D. Chowdhury, A. Chubokov, R. Fernandes, M. Gerlach, S. Kivelson, A. Klein, Z.-Y. Meng, M. Metlitski, S. Sachdev, K. Sun, X.-Y. Xu, Xiaoyu Wang, and Yuxuan Wang for collaboration on the numerical investigations reviewed here and on related topics. S.L. acknowledges support from the Gordon and Betty Moore Foundation's EPiQS Initiative. Y.S. is supported by the Department of Energy, Office of Science, Basic Energy Sciences, Materials Sciences and Engineering Division, under Contract DEAC02-76SF00515 and by the Zuckerman STEM Leadership Program. We also gratefully acknowledge allocation of the much-needed computing time on the CHEOPS cluster at RRZK Cologne, the JURECA cluster at the Forschungszentrum Jülich, the SIMES cluster at SLAC, and the ATLAS cluster at the Weizmann Institute.

LITERATURE CITED

1. Mathur N, Grosche F, Julian S, Walker I, Freye D, et al. 1998. *Nature* 394:39
2. Gegenwart P, Custers J, Geibel C, Neumaier K, Tayama T, et al. 2002. *Phys. Rev. Lett.* 89:056402

3. Custers J, Gegenwart P, Wilhelm H, Neumaier K, Tokiwa Y, et al. 2003. *Nature* 424:524
4. Paglione J, Tanatar MA, Hawthorn DG, Boaknin E, Hill RW, et al. 2003. *Phys. Rev. Lett.* 91:246405
5. Bianchi A, Movshovich R, Vekhter I, Pagliuso P, Sarrao J. 2003. *Phys. Rev. Lett.* 91:257001
6. Park T, Ronning F, Yuan HQ, Salamon MB, Movshovich R, et al. 2006. *Nature* 440:65–68
7. Gegenwart P, Si Q, Steglich F. 2008. *Nat. Phys.* 4:186–97
8. Nakatsuji S, Kuga K, Machida Y, Tayama T, Sakakibara T, et al. 2008. *Nat. Phys.* 4:603
9. Matsumoto Y, Nakatsuji S, Kuga K, Karaki Y, Horie N, et al. 2011. *Science* 331:316–19
10. Landaeta JF, Subero D, Catalá D, Taylor SV, Kimura N, et al. 2018. *Phys. Rev. B* 97:104513
11. Hashimoto K, Cho K, Shibauchi T, Kasahara S, Mizukami Y, et al. 2012. *Science* 336:1554–57
12. Shibauchi T, Carrington A, Matsuda Y. 2014. *Annu. Rev. Condens. Matter Phys.* 5:113–35
13. Chu JH, Kuo HH, Analytis JG, Fisher IR. 2012. *Science* 337:710–12
14. Kuo HH, Chu JH, Palmstrom JC, Kivelson SA, Fisher IR. 2016. *Science* 352:958–62
15. Gallais Y, Fernandes RM, Paul I, Chauvière L, Yang YX, et al. 2013. *Phys. Rev. Lett.* 111:267001
16. Thorsmølle VK, Khodas M, Yin ZP, Zhang C, Carr SV, et al. 2016. *Phys. Rev. B* 93:054515
17. Böhmer AE, Burger P, Hardy F, Wolf T, Schweiss P, et al. 2014. *Phys. Rev. Lett.* 112:047001
18. Motoyama E, Yu G, Vishik I, Vajk O, Mang P, Greven M. 2007. *Nature* 445:186
19. Armitage N, Fournier P, Greene R. 2010. *Rev. Mod. Phys.* 82:2421
20. Daou R, Cyr-Choinière O, Laliberté F, LeBoeuf D, Doiron-Leyraud N, et al. 2009. *Phys. Rev. B* 79:180505
21. Ramshaw BJ, Sebastian SE, McDonald RD, Day J, Tan BS, et al. 2015. *Science* 348:317–20
22. Daou R, Doiron-Leyraud N, LeBoeuf D, Li SY, Laliberte F, et al. 2009. *Nat. Phys.* 5:31–34
23. Wölfle P, Abrahams E. 2011. *Phys. Rev. B* 84:041101
24. Hertz JA. 1976. *Phys. Rev. B* 14:1165–84
25. Moriya T. 1985. *Spin Fluctuations in Itinerant Electron Magnetism*. Berlin: Springer
26. Millis AJ. 1993. *Phys. Rev. B* 48:7183–96
27. Vojta M, Zhang Y, Sachdev S. 2000. *Phys. Rev. B* 62:6721–44
28. Assaad FF, Herbut IF. 2013. *Phys. Rev. X* 3:031010
29. Li ZX, Jiang YF, Jian SK, Yao H. 2017. *Nat. Commun.* 8:314
30. Altshuler B, Ioffe L, Millis A. 1994. *Phys. Rev. B* 50:14048
31. Nayak C, Wilczek F. 1994. *Nuclear Phys. B* 430:534–62
32. Nayak C, Wilczek F. 1994. *Nuclear Phys. B* 417:359–73
33. Altshuler BL, Ioffe LB, Millis AJ. 1995. *Phys. Rev. B* 52:5563–72
34. Chakravarty S, Norton R, Syljuasen O. 1995. *Phys. Rev. Lett.* 74:1423–26
35. Castellani C, DiCastro C, Grilli M. 1995. *Phys. Rev. Lett.* 75:4650–53
36. Abanov A, Chubukov AV. 1999. *Phys. Rev. Lett.* 83:1652–55
37. Abanov A, Chubukov A. 2000. *Phys. Rev. Lett.* 84:5608
38. Abanov A, Chubukov A, Schmalian J. 2003. *Adv. Phys.* 52:119
39. Metzner W, Rohe D, Andergassen S. 2003. *Phys. Rev. Lett.* 91
40. Abanov A, Chubukov A. 2004. *Phys. Rev. Lett.* 93:255702
41. Pankov S, Florens S, Georges A, Kotliar G, Sachdev S. 2004. *Phys. Rev. B* 69:054426
42. Lawler MJ, Barci DG, Fernández V, Fradkin E, Oxman L. 2006. *Phys. Rev. B* 73:085101
43. Rech J, Pepin C, Chubukov AV. 2006. *Phys. Rev. B* 74:195126
44. v. Löhneysen H, Rosch A, Vojta M, Wölfle P. 2007. *Rev. Mod. Phys.* 79:1015
44a. Aji V, Varma CM. 2007. *Phys. Rev. Lett.* 99:067003
45. Lee SS. 2009. *Phys. Rev. B* 80:165102
46. Zacharias M, Woelfle P, Garst M. 2009. *Phys. Rev. B* 80
47. Metlitski M, Sachdev S. 2010. *Phys. Rev. B* 82:075127
48. Metlitski M, Sachdev S. 2010. *Phys. Rev. B* 82:075128
49. Mross DF, McGreevy J, Liu H, Senthil T. 2010. *Phys. Rev. B* 82:045121
50. Maslov DL, Chubukov AV. 2010. *Phys. Rev. B* 81:045110
51. Dalidovich D, Lee SS. 2013. *Phys. Rev. B* 88:245106
52. Efetov K, Meier H, Pépin C. 2013. *Nat. Phys.* 9:442
53. Abrahams E, Schmalian J, Wölfle P. 2014. *Phys. Rev. B* 90:045105

54. Fitzpatrick AL, Kachru S, Kaplan J, Raghu S. 2014. *Phys. Rev. B* 89:165114
55. Meier H, Pépin C, Einenkel M, Efetov K. 2014. *Phys. Rev. B* 89:195115
56. Holder T, Metzner W. 2015. *Phys. Rev. B* 92:041112
57. Wang Y, Chubukov AV. 2015. *Phys. Rev. B* 92:125108
58. Raghu S, Torroba G, Wang H. 2015. *Phys. Rev. B* 92:205104
59. Varma C. 2015. *Phys. Rev. Lett.* 115:186405
59a. Varma CM. 2016. *Rep. Progr. Phys.* 79(8):082501
60. Schlief A, Lunts P, Lee SS. 2017. *Phys. Rev. X* 7:021010
61. Lee S-S. 2018. *Annu. Rev. Condens. Matter Phys.* 9:227–44
62. Meszena B, Säterskog P, Bagrov A, Schalm K. 2016. *Phys. Rev. B* 94:115134
63. Säterskog P. 2018. *SciPost Phys.* 4:015
64. Berg E, Metlitski MA, Sachdev S. 2012. *Science* 338:1606–9
65. Schattner Y, Lederer S, Kivelson SA, Berg E. 2016. *Phys. Rev. X* 6:031028
66. Li ZX, Wang F, Yao H, Lee DH. 2016. *Sci. Bull.* 61:925–30
67. Schattner Y, Gerlach MH, Trebst S, Berg E. 2016. *Phys. Rev. Lett.* 117:097002
68. Gerlach MH, Schattner Y, Berg E, Trebst S. 2017. *Phys. Rev. B* 95:035124
69. Lederer S, Schattner Y, Berg E, Kivelson SA. 2017. *PNAS* 114:4905–10
70. Wang X, Wang Y, Schattner Y, Berg E, Fernandes RM. 2018. *Phys. Rev. Lett.* 120:247002
71. Wang X, Schattner Y, Berg E, Fernandes RM. 2017. *Phys. Rev. B* 95:174520
72. Xu XY, Sun K, Schattner Y, Berg E, Meng ZY. 2017. *Phys. Rev. X* 7:031058
73. Li ZX, Wang F, Yao H, Lee DH. 2017. *Phys. Rev. B* 95:214505
74. Gazit S, Randeria M, Vishwanath A. 2017. *Nat. Phys.* 13:484–90
75. Loh EY, Gubernatis JE, Scalettar RT, White SR, Scalapino DJ, Sugar RL. 1990. *Phys. Rev. B* 41:9301–7
76. Fitzpatrick AL, Kachru S, Kaplan J, Raghu S, Torroba G, Wang H. 2015. *Phys. Rev. B* 92:045118
77. Lunts P, Schlief A, Lee SS. 2017. *Phys. Rev. B* 95:245109
78. Scalapino D, Loh E Jr., Hirsch J. 1986. *Phys. Rev. B* 34:8190
78a. Miyake K, Schmitt-Rink S, Varma CM. 1986. *Phys. Rev. B* 34:6554(R)
79. Monthoux P, Balatsky A, Pines D. 1991. *Phys. Rev. Lett.* 67:3448
80. Abanov A, Chubukov AV, Schmalian J. 2001. *Europhys. Lett.* 55:369–75
81. Metlitski MA, Sachdev S. 2010. *New J. Phys.* 12:105007
82. Metlitski MA, Mross DF, Sachdev S, Senthil T. 2015. *Phys. Rev. B* 91:115111
83. Wang Y, Abanov A, Altshuler BL, Yuzbashyan EA, Chubukov AV. 2016. *Phys. Rev. Lett.* 117:157001
84. Lederer S, Schattner Y, Berg E, Kivelson SA. 2015. *Phys. Rev. Lett.* 114:097001
85. Maier TA, Scalapino DJ. 2014. *Phys. Rev. B* 90:174510
86. Chubukov AV, Pépin C, Rech J. 2004. *Phys. Rev. Lett.* 92:147003
87. Wang Y, Agterberg DF, Chubukov A. 2015. *Phys. Rev. Lett.* 114:197001
88. Gubernatis J, Kawashima N, Werner P. 2016. *Quantum Monte Carlo Methods: Algorithms for Lattice Models*. Cambridge, UK: Cambridge Univ. Press
89. Landau DP, Binder K. 2000. *A Guide to Monte Carlo Simulations in Statistical Physics*. Cambridge, UK: Cambridge Univ. Press
90. Troyer M, Wiese UJ. 2005. *Phys. Rev. Lett.* 94:170201
91. Lang GH, Johnson CW, Koonin SE, Ormand WE. 1993. *Phys. Rev. C* 48:1518–45
92. Wu C, Zhang SC. 2005. *Phys. Rev. B* 71:155115
93. Chandrasekharan S. 2010. *Phys. Rev. D* 82:025007
94. Huffman EF, Chandrasekharan S. 2014. *Phys. Rev. B* 89:111101
95. Li ZX, Jiang YF, Yao H. 2015. *Phys. Rev. B* 91:241117
96. Li ZX, Jiang YF, Yao H. 2016. *Phys. Rev. Lett.* 117:267002
97. Wei Z, Wu C, Li Y, Zhang S, Xiang T. 2016. *Phys. Rev. Lett.* 116:250601
98. Wang L, Liu YH, Iazzi M, Troyer M, Harcos G. 2015. *Phys. Rev. Lett.* 115:250601
99. Wei ZC. 2017. *arXiv:1712.09412*
100. Blankenbecler R, Scalapino DJ, Sugar RL. 1981. *Phys. Rev. D* 24:2278
101. Scalettar RT, Loh EY, Gubernatis JE, Moreo A, White SR, et al. 1989. *Phys. Rev. Lett.* 62:1407

102. Assaad FF. 2002. In *Quantum Simulations of Complex Many-Body Systems: From Theory to Algorithms*, ed. J Grotendorst, D Marx, A Muramatsu, pp. 99–156. Julich, Germ.: John von Neumann Institute for Computing
103. Assaad FF. 2002. *Phys. Rev. B* 65:115104
104. Liu J, Shen H, Qi Y, Meng ZY, Fu L. 2017. *Phys. Rev. B* 95:241104
105. Liu ZH, Xu XY, Qi Y, Sun K, Meng ZY. 2018. *Phys. Rev. B* 98:045116
106. Xu XY, Qi Y, Liu J, Fu L, Meng ZY. 2017. *Phys. Rev. B* 96:041119
107. Liu ZH, Xu XY, Qi Y, Sun K, Meng ZY. 2018. arXiv:1801.00127
108. Bauer C, Schattner Y, Berg E, Trebst S. 2018. In preparation
109. Punk M. 2016. *Phys. Rev. B* 94:195113
110. Klein A, Chubukov A. 2017. *Phys. Rev. B* 96:041125
111. Trivedi N, Randeria M. 1995. *Phys. Rev. Lett.* 75:312–15
112. Gubernatis J, Jarrell M, Silver R, Sivia D. 1991. *Phys. Rev. B* 44:6011